Investigation on the potential of PCB winding technology for high-dynamic and high-precision linear actuators

Guillaume Colinet [1], William Lamberts [1], François Baudart [2], Bruno Dehez [1]

[1] *Mechatronic, Electrical Energy, Dynamic systems (MEED)*
Institute of Mechanics, Materials and Civil Engineering (IMMC)
Université catholique de Louvain (UCL)
[2] *Mirmex Motor SA*

***Abstract*—Slotless linear permanent magnet actuators are widely used in applications that require a high dynamics and precision in the motion. However, the windings limit the performances of such motors. A new technology, that consists in printing the windings on a PCB has shown promising results for rotary motor, as well as for tubular linear motor. This paper proposes to study the potential of this technology for a planar linear motor. To that end, an analytical model of the actuator is first presented, from which performance criteria related to the force density and to the force ripple are derived. Then, using those criteria, the results of a bi-objective optimization, based on an existing linear actuator, are presented. Finally, a first prototype is built and characterized in a test bench with a view to validate the optimization results and to make a comparison with the existing motor.**

I. Introduction

Linear permanent magnet (PM) actuators are widely used in a variety of applications that require linear movements as it offers significant advantages in terms of dynamics. Among the various topologies of linear PM actuators, the slotted linear motor has the advantage of a high force density, and therefore high dynamics but suffers from cogging force [1] which deteriorates the precision of the motion. For high precision applications, a slotless topology is therefore often prefered [2]. More specifically, planar linear actuators with a U-channel stator and a moveable winding meets the requirements in terms of precision, accepting a lower dynamics [2], [3].

Usually, the windings of slotless topologies are made of copper wires wound in a concentrated configuration. However a new technology that consists in printing the winding on PCBs [4] could bring interesting improvements both in terms of force density and force ripple. Indeed this technology demonstrated significant improvements of the motor constant for radial flux rotary machines by introducing topologies of overlapping windings that are inconceivable with the traditionnal wire technology. [5], [6], [7]. It has also shown the possibility to obtain a sinusoidal back-emf which could eliminate the ripple on the force in case of AC supply, in a tubular linear actuator [8].

In this context, the present paper proposes to study the potential of the technology proposed in [7] for a planar linear actuator. In order to reach this goal, an electromagnetic model is build and links the internal parameters of the actuator to performance criteria related to the force density and the force ripple. Based on this model a bi-objective optimization is performed, considering only the parameters related to the shape of the winding as optimization parameters, the other parameters being fixed to the ones of an existing actuator, also made of PCB windings but with a concentrated configuration. Finally, the results of the optimization process are used to build a prototype of the winding, which is characterized in a test bench and then compare, on the basis of the two performance criteria, to the existing actuator.
This paper has the following structure. Section II presents a description of the actuator, as well as the parameters that characterize the winding. Section III provides the electromagnetic model. Section IV presents the performance criteria related to the force density and the force ripple. From those criteria, the results of a bi-objective optimization are shown and then discussed. Section V presents the description of the test bench, the characterization of the winding prototype and its comparison with an existing actuator.

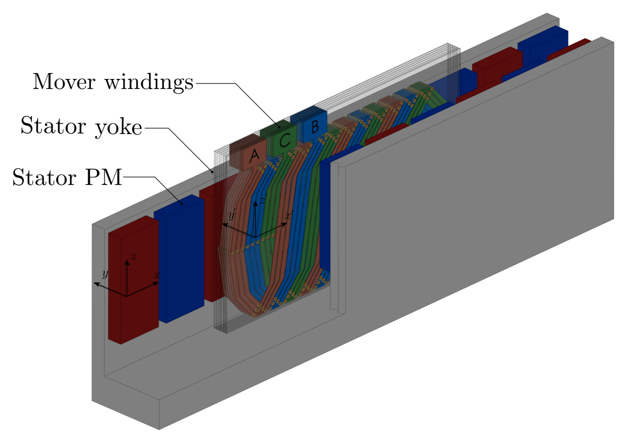

Fig. 1. 3D view of the actuator.

II. Actuator description and parametrization

The actuator that is considered in this study is illustrated in Fig. 1. The stator is a double-sided topology with permanent magnets mounted on a U-channel yoke. Each north pole is facing a south pole on the other side. The moving part of the actuator is made of a three-phase distributed winding. In contrast with radial flux rotary machines with a PCB having an optimized shape [6], N_l independant PCBs separated by an insulation layer, are stacked one on top of each other.

Each PCB is made of a double-sided copper clad with copper tracks printed on both side according to the layout presented in Fig. 2.

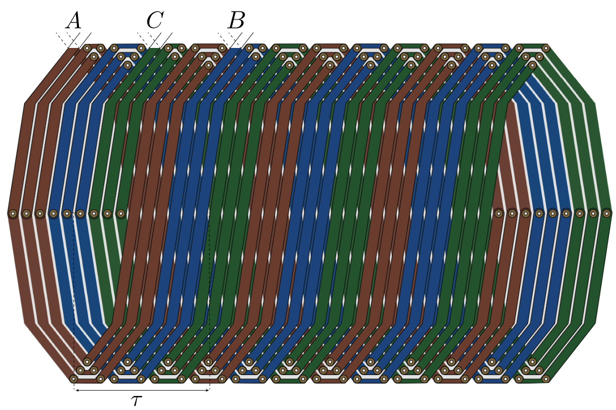

Fig. 2. Phase of a winding layer formed of $N_c = 4$ coils ($N_t = 3$).

A PCB, whose winding pitch equals to the magnet pitch of the PM τ, is characterized by N_p, the number of poles and by N_t, the number of loops forming a pole. The shape of these loops is made of a succession of linear segments whose end positions are also parameters of the winding. As shown in Fig. 3, each segment is defined by the coordinates of its extremities.

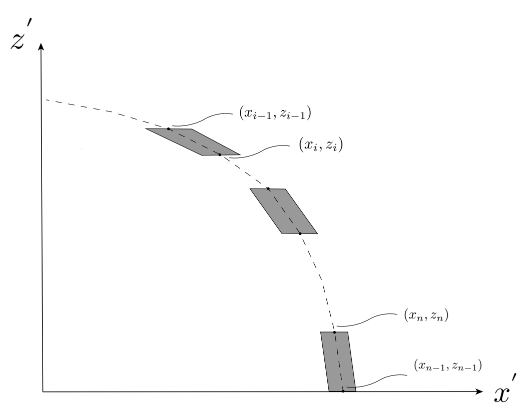

Fig. 3. Discretization of a loop.

Two coordinate systems are used. The first is fixed to the stator, and the second is fixed to the mover. These are related thanks to the following coordinate transformation:

$$(x', y', z') = (x - q, y, z)$$

with q the relative position between the stator and the mover.

III. Modeling

Evaluating the performances of the actuator requires a modeling of its characteristics. In this section, an electromagnetic model of the actuator is presented. This latter allows to predict the magnetic properties of the actuator, namely the distribution of the magnetic flux density of the PM and the magnetic flux linked by the windings, this latter together with the current that flows in the windings being responsible of the force that the actuator can develop. Furthermore, as the force produced by the motor is proportional to the current in the windings, the model provides also an estimation of the electrical resistance in order to evaluate the Joules losses.

A. *Magnetic flux density*

Only the y-component of the magnetic flux density due to the PM is modeled as it is the one producing the desired component of the force, being in the x-direction. The methodology used for obtaining the latter is the Fourier approach described in [9]. In our specific case, the underlying hypotheses are the following:

1) Armature reaction field is neglected.
2) The end effects close the sides of the magnets in the $\mathbf{z}$-direction are neglected.
3) The PM are distributed periodically along the $\mathbf{x}$-axis.
4) The relative permeability μ_r of the air and the magnets is assumed equal to 1.
5) The magnetic saturation is neglected.

According to those assumptions, the original 3D model can be reduced to a 2D periodical problem with four regions, as depicted in Fig. 4.

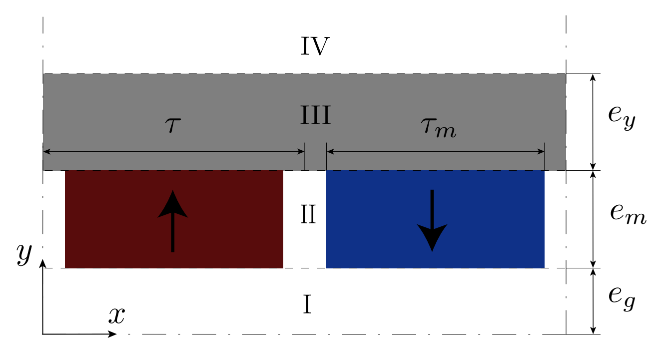

Fig. 4. 2D analytical model and dimensions.

In [10], the autors considered the same configuration but supposed the magnetic permeability of the stator yoke infinite, allowing them to reduce the number of regions to only two, i.e. the air-gap region (I) and the PM region (II), discarding the iron region (III) and the external air region (IV).

In each region, the Maxwell equations can be reduced either to the Laplace equation:

$$\frac{\partial^2 A_z}{\partial x^2} + \frac{\partial^2 A_z}{\partial y^2} = 0 \tag{1}$$

if there are no PM region (II), or to the Poisson equation:

$$\frac{\partial^2 A_z}{\partial x^2} + \frac{\partial^2 A_z}{\partial y^2} = -\mu_0 \frac{\partial M_y}{\partial x} \tag{2}$$

with A_z the non-null component of the magnetic vector potential and M_y the y-component of the magnetization. Solving the linear system obtained by applying boundary conditions allows to find an analytical expression of the magnetic vector potential, from which an expression of the y-component of the magnetic flux density is deduced.

$$B_{y\mathrm{I}} = \sum_{n=1}^{\infty} \beta_n \cosh(w_n y) \sin(w_n x) \tag{3}$$

with w_n the spatial frequency:

$$w_n = \frac{k_n \pi}{\tau} = \frac{(2n-1)\pi}{\tau} \tag{4}$$

and β_n:

$$\begin{aligned}
\beta_n = \ & \Big\{ 2\, B_r(\mu_f+1)\exp\Big(-w_n e_g\Big) \\
& + B_r(\mu_f+1)^2 \exp\Big(w_n(e_m - e_g)\Big) \\
& + B_r(\mu_f^2-1)\exp\Big(-w_n(e_m+e_g)\Big) \\
& + 2\, B_r(\mu_f-1)\exp\Big(-w_n(2e_y+e_g)\Big) \\
& + B_r(\mu_f-1)^2 \exp\Big(w_n(e_m-2e_y-e_g)\Big) \\
& + B_r(1-\mu_f^2)\exp\Big(-w_n(e_m+2e_y+e_g)\Big)\Big\} \times \frac{-1}{D} \\
D = \ & (1+\mu_f)^2 + (1-\mu_f^2)\exp\Big(-2w_n e_g\Big) \\
& - (\mu_f-1)^2 \exp\Big(-2w_n e_y\Big) \\
& + (\mu_f^2-1)\exp\Big(-2w_n(e_y+e_g)\Big).
\end{aligned}$$

In order to validate the predictions from the model, the magnetic flux density is also estimated with a 2D FEM model using the FEMM software. Using the parameters given in Table I and Table II, the results are shown in Fig. 5 and it can be seen that the proposed model is in good agreement with the 2D FEM model.

To emphasize the importance of the end-effects in the z-direction, that have been neglected in the model that was previously presented, a comparison with a 3D FEM model has been done. It showed that the analytical model highly overestimates the value of the magnetic flux density close to the edges of the PM. However, over the height of a PM, a mean error of about 8% is obtained.

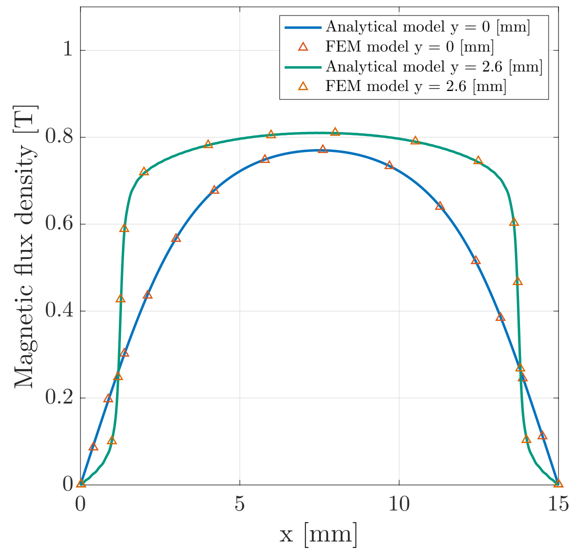

Fig. 5. Magnetic flux density in the airgap.

B. Magnetic flux

The magnetic flux linked by one winding phase has the following form:

$$\Psi(q) = \sum_{n=1}^{\infty} \hat{\Psi}_n \sin(w_n q + \phi) \tag{5}$$

where $\hat{\Psi}_n$ is the amplitude of the harmonic of order k_n of the phase flux. Because of the dependency on y of the magnetic flux density, each PCB layer links a different flux amplitude, which is given by:

$$\hat{\Psi}_n = \sum_{k=1}^{N_l} N_p \hat{\Psi}_{p,n}(y_k) \tag{6}$$

where $\hat{\Psi}_{p,n}(y_k)$ denotes the amplitude of the flux linked by one winding pole of a layer located in $y = y_k$. Due to the symmetry of the winding, the flux is evaluated only on one quarter of a winding pole, by summing the contribution of each segment. The contribution of a segment is computed through the line integral of the magnetic vector potential in a way similar to the one presented in [5] for BLDC motors. However it is adapted such that the magnetic flux density equals zero for the part of the winding located outside of the PM along the z direction.

A comparison of the results with a 3D FEM model shows that the analytical model overestimates the magnetic flux by approximately 2%.

C. Force

In three-phase slotless PM machines, the force is purely eletrodynamic and is given by the general expression:

$$F(q) = I_a \frac{d\Psi_a(q)}{dq} + I_b \frac{d\Psi_b(q)}{dq} + I_c \frac{d\Psi_c(q)}{dq} \tag{7}$$

with Ψ_i the magnetic flux linked by the winding phase *i* and I_i the current flowing in the phase *i* . Considering the flux in the three winding phases are exactly 120° shifted each other and the supply currents are three-phase currents in phase with the back-emf, the resulting force is:

$$F(q) = \frac{3\sqrt{2}}{2}\frac{\pi}{\tau}I_{rms}\hat{\Psi}_1 + \hat{I}\sum_{j=1}^{\infty} A_j \cos\left(\frac{2j\pi}{\tau}q\right) \quad (8)$$

where A_j is the amplitude of j^{th} harmonic of the force normalized by the peak current $\hat{I}$. This form will be later used for the analysis of the force ripple.

D. Phase resistance

The resistance of a phase is made of the contribution of the N_p poles, over the N_l layers. Due to the symmetry of a pole, his contribution is evaluated on only one quarter of a pole. The phase resistance is therefore expressed as:

$$R_{ph} = 4N_p N_l R_{qp} \quad (9)$$

where R_p is the resistance of one quarter of a winding pole and is computed by summing the contributions of each segment, assuming a constant current density as proposed in [5].

IV. Optimization

A. Objective functions

The dynamics of an electrical machine is linked to the mean force it can develop. However as the mean force is proportional to the current amplitude, it is generally limited by the Joule losses. This is why, a criterion generally used is the motor constant k_p defined as:

$$k_p = \frac{k_F}{\sqrt{R_{ph}}} \quad (10)$$

where k_F is the force constant, linking the mean force to the RMS value of the current and is in accordance with (8):

$$k_f = \frac{3\sqrt{2}}{2}\frac{\pi}{\tau}\hat{\Psi}_1 \quad (11)$$

Indeed, by multiplying both the numerator and the denominator in (10) by the RMS value of the current, the motor constant reveals to be proportional to the ratio between the mean force and the square root of the Joule losses.

Regarding the precision of the motion generated by an electrical machine, it is limited by the prominence of the force ripple. A classic criterion used in the literature is the total harmonic distortion (THD) of the back electromotive force [11]. This distortion index relies on the fact that only the fundamental flux harmonic $\hat{\Psi}_1$ produces a non-zero mean force. The THD of the phase flux can thus be defined as:

$$THD_\Psi = \frac{\sqrt{\sum\limits_{k_n=5,7,11,13,17,..}^{\infty} (w_n \hat{\Psi}_n)^2}}{\frac{\pi}{\tau}\hat{\Psi}_1} \quad (12)$$

where only the flux harmonics contributing to the force are involved.

Nevertheless, one can directly evaluate the THD of the force:

$$THD_F = \frac{\sqrt{\sum\limits_{j=1}^{\infty} A_j^2}}{k_F} \quad (13)$$

A third criterion is the ratio between the peak amplitude of the force oscillations and the average force:

$$O_F = \frac{\max(F) - \min(F)}{F_{avg}} \quad (14)$$

Fig. 6 compares the three performance indexes normalized by their respective maximum value as function of the PM fill factor for a k_p-optimal winding, the other parameters than τ_m being the ones in Table I and Table II. A clear correlation is observed between THD_F and O_F, the slight difference resulting of the fact that THD_F takes into account the whole spectrum of the force harmonics. The THD_Ψ curve differs from the other indexes. Particularly, the respective minima do not coincide. As a result, the total harmonic distortion of the force appears to be the best index to quantify the force oscillations and will thus be preferred for the optimization.

In conclusion, for optimizing both the dynamic and the precision of the motion, a multi-objective optimization combining both the motor constant k_p and the THD of the force THD_F as objective functions seems the most apropriate.

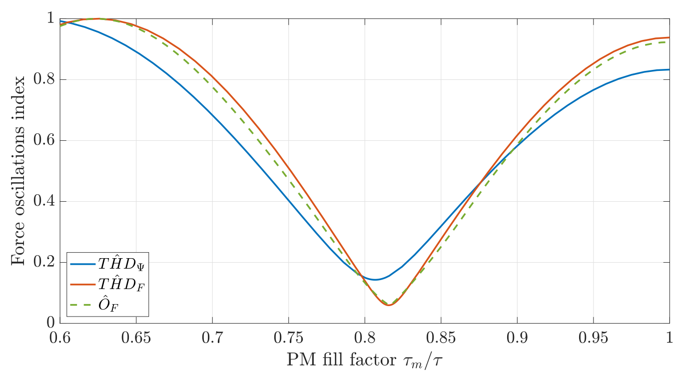

Fig. 6. Comparison of the force oscillations indexes with varying PM fill factor.

B. Results

In order to demonstrate the potential of the PCB winding technology, it has been decided to limit the optimization parameters to those linked to the winding shape. Among the other actuator parameters, the stator parameters are given in Table I and have been fixed equal to those of an existing commercial linear actuator. Regarding the parameters related to the winding, excluding those defining its shape, they are given in Table II and have been determined considering a specific copper clad and bondply, so as to keep the same external dimensions as the existing actuator.

The number of turns N_t has a major influence for high operating speeds since it directly impacts the supply voltage and the eddy current losses in the copper tracks [12]. As no particular speed profile is targeted in the present work, N_t is fixed arbitrarily.

The optimization of the winding shape is performed by using the NSGA-II genetic algorithm as proposed in [5].

TABLE I
STATOR PARAMETERS

Parameter	Symbol	Value	Unit
Half airgap thickness	e_g	2.7	mm
PM thickness	e_m	4	mm
Yoke thickness	e_y	4	mm
PM height	h_m	30	mm
PM pole pitch	τ	15	mm
PM width	τ_m	12.5	mm
PM remanent flux density	B_r	1.39	T
Yoke relative permeability	μ_f	5000	–

TABLE II
WINDING PARAMETERS

Parameter	Symbol	Value	Unit
Number of poles per layer phase	N_p	4	–
Number of layers	N_l	16	–
Number of loops per coil	N_t	3	–
Copper thickness	t_c	90	μm
Insulation thickness	t_i	50	μm
Substrate thickness	t_s	25	μm

Fig. 7 presents the optimization results in a plane with growing k_p as ordinate and decreasing THD_F as abscissa. The bi-objective optimization process consists of about 20 optimizations with different weights given to the two performance criteria in the objective function as indicated by the colorbar. The Pareto front, composed of thousands of motors achieving one of the best compromises; is found between the two extrema $(k_p, THD_F) = (8.617, 0.06)$ and $(k_p, THD_F) = (8.46, 1.35 \times 10^{-4})$. This curve allows to find the best motor for a given application by choosing a maximum acceptable THD value or a minimum motor constant.
For the experimental validation adressed in the next section, the motor having $(k_p, THD_F) = (8.46, 1.35 \times 10^{-4})$ is selected. The coil shape of some motors selected at regular motor constant variation along the Pareto frontier is drawn in Fig. 8. It can be seen that the shape is more curved when the motor constant is higher, which is consistent with the fact that more magnetic flux is linked by the winding. The force generated by these motors is plotted in Fig. 9 to give a more intuitive visualization of the results. It illustrates the tradeoff between a high mean force and low oscillations of the force.

V. EXPERIMENTAL VALIDATION

In order to validate the predictions from the models but also the potential of the PCB winding technology for obtaining high-dynamic and high-precision linear actuator, a test bench has been build. Using this test bench, a prototype of winding is first characterized and the possible deviations from the models are discussed and then a comparison of the performances of this prototype with a commercial actuator is provided. Comparing the performances of the two actuators requires a

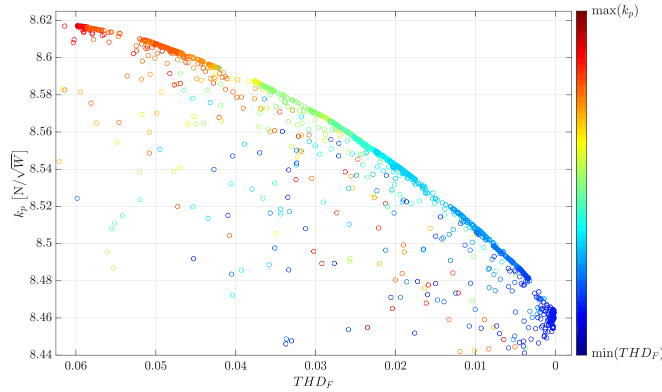

Fig. 7. Bi-objective optimization for $\tau_m/\tau = 25/30$.

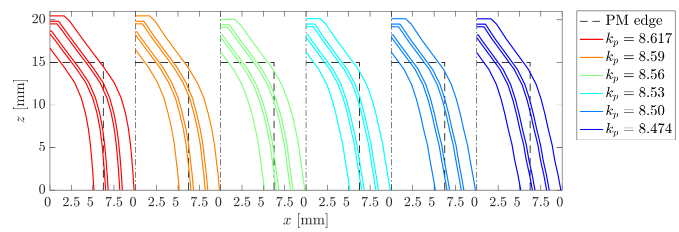

Fig. 8. Coil shape evolution along the Pareto frontier.

measure of the most relevant optimization criteria, namely the motor constant and the THD of the force. In this section, a description of the test bench is first provided. Then it is explained how the measure of the optimization criteria is achieved. Finally, the results are presented and discussed.

A. Description of the test bench

The test bench that has been realized is shown in Fig. 10. It is made of several elements, labeled in Fig. 11 and each one of those elements are referenced in Table III

TABLE III
LIST OF THE ELEMENTS OF THE PROTOTYPE

n°	Part
1	Bottom aluminum plate
2	Rail of magnets
3	Linear guide and preconstrained cart
4	Shock-absorbing stop
5	Cable carrier
6	Support piece of the readhead
7	Readhead of the positioning system
8	Optical scale of the positioning system
9	Support piece of the two PCB windings
10	Clamping piece for the developed PCB windings
11	Proposed windings
12	Commercial windings

Two identical rails of PM are symetrically placed on both sides of a linear guide on which a moveable cart is preconstrained. On this latter, both windings are fixed thanks to a support piece. This symmetric structure allows to place in competition the proposed winding and the commercial winding. For driving the motion, an IPOS8020 controller from

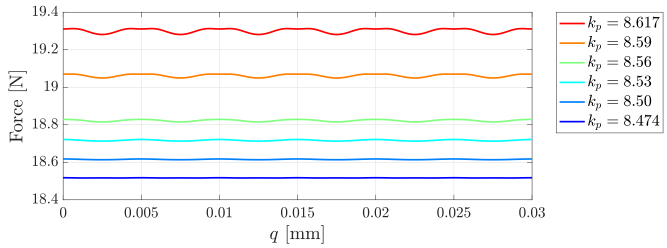

Fig. 9. Force evolution along the Pareto frontier.

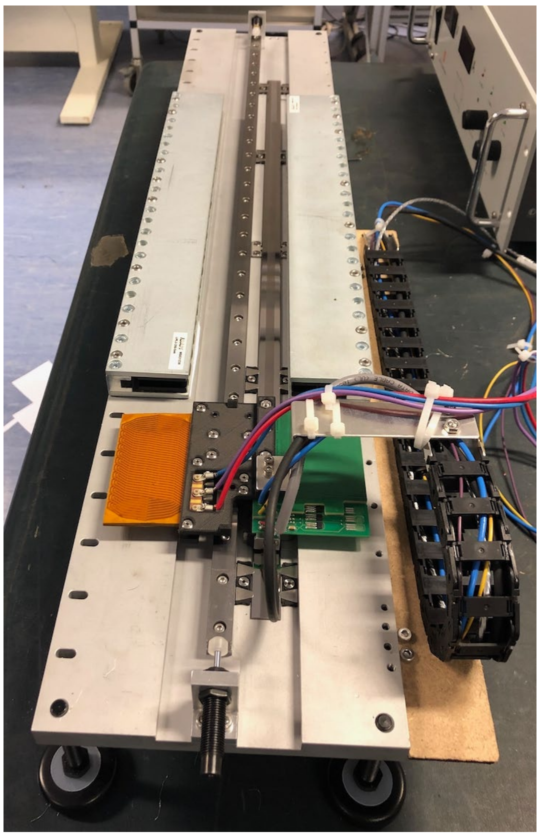

Fig. 10. Picture of the test bench.

Technosoft as well as a positionning system from *Renishaw* are used. The positionning system is made of an optical scale and a readhead placed on the support piece.

B. Measurements

An estimation of the optimization criteria requires to perfom dedicated measurements. For the motor constant, a measure of the electrical resistance, as well as the mean force developed by the actuator is required. Concerning the total harmonic distorsion of the force, a measure of the ripple on the force is required. However, an experimental measure of the force would have required a force sensor, which is unfortunately not provided in the test bench. Furthermore, the accuracy of the measure would have been impacted by the quality of the controller. As a consequence, is has been prefered to estimate the force developed by the actuator

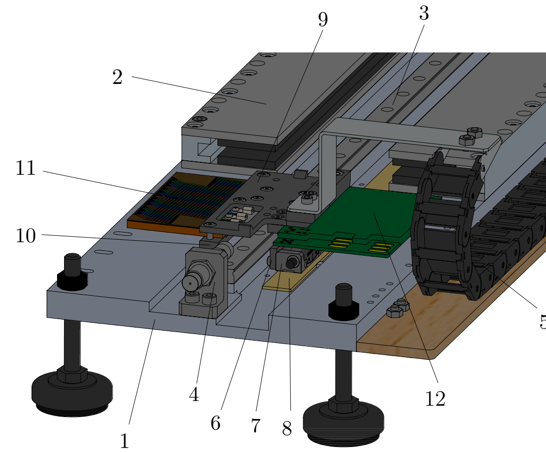

Fig. 11. Constitutive elements of the test-bench.

through a measure of the magnetic flux linked by the windings. Indeed the mean force, which is directly linked to the force constant given by (11), is related to the fundamental of the magnetic flux. Concerning the oscillations on the force, they can be evaluated through the harmonics of the magnetic flux using THD_{Ψ}.

The way the fundamental and the harmonics of the magnetic flux are measured is now described. As a first step, a simultaneous measurement of the position and the back electromotive force induced on one phase of a winding, while it is passively driven by the other one, is performed. For achieving this a 4 channel oscilloscope has been used in order to both measure the two quadrature signals from the position sensor, and the back-emf on two lines of the winding. The next step consists in a numerical processing of these data. Knowing the resolution of the position sensor and by detecting the rising and falling edge of the two quadrature signals, the evolution of the position with time can be retrieved. Concerning the magnetic flux, it is obtained by doing a numerical integration of the back-emf on the two lines. With the position and the magnetic flux, the last step consists in a Fourier analysis in order to obtain the amplitude of the spatial harmonics of the magnetic flux. From these harmonics, through (11) and (12) respectively, both the force constant k_F and the total harmonic distortion on the flux THD_{Ψ} can be derived.

C. Results

Fig. 12 shows the measure of the back-emf induced on one phase of the prototype of the proposed winding and of the position with respect to the time. The result of a numerical integration on the back-emf is given in Fig. 13. Obviously, the shape of the magnetic flux with time is related to the position profile and therefore it would have been meaningless to perform a Fourier analysis directly on it. Combining the evolution of the position with time and the evolution of the magnetic flux with time, and keeping only an integer number of periods for the purpose of a Fourier analysis, Fig. 14

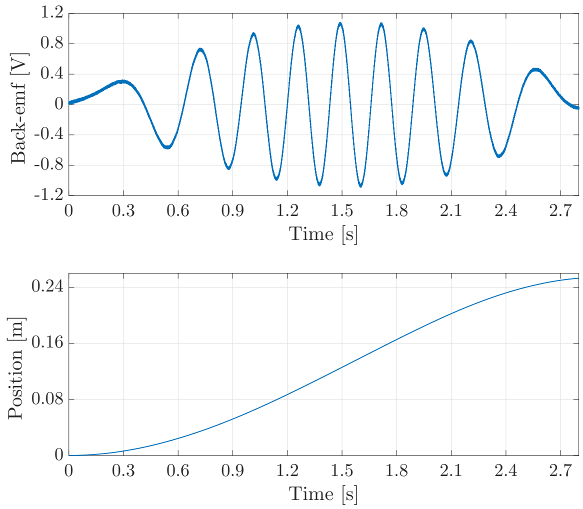

Fig. 12. Evolution of back-emf and position with time.

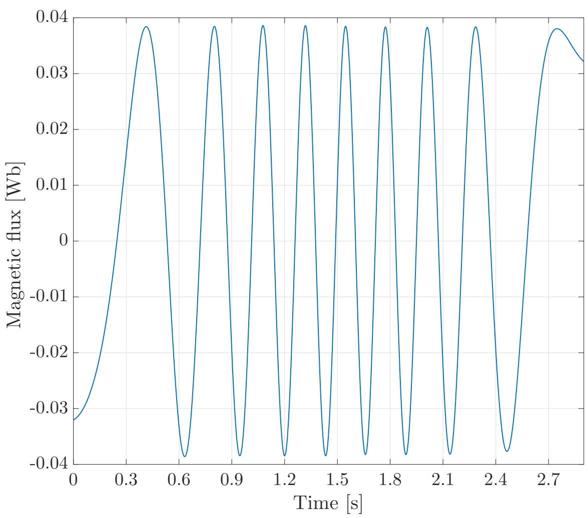

Fig. 13. Evolution of magnetic flux with time.

is obtained. It can be seen that the magnetic flux has a sinusoidal shape, meaning that the fundamental component is highly dominant. From a Fourier analysis, the force constant of the two actuators can be retrieved: for the proposed motor $k_f = 17.04$ $[N/A_{rms}]$ and for the existing motor $k_f = 13.2$ $[N/A_{rms}]$. Comparing the value of the force constant of the proposed actuator to the one predicted by the model, gives an error of 4.3%. A fraction of this error is due to the overestimation of the magnetic flux. Concerning the other harmonics, used for evaluating THD_{Ψ}, these proved to be too weak to be able to be estimated with sufficient precision. The phase resistance of the considered winding has also been measured using a *HM8118 LCR Bridge/Meter*. A relative difference of 25% is observed between the prediction and the measured value. About 60% of this difference comes

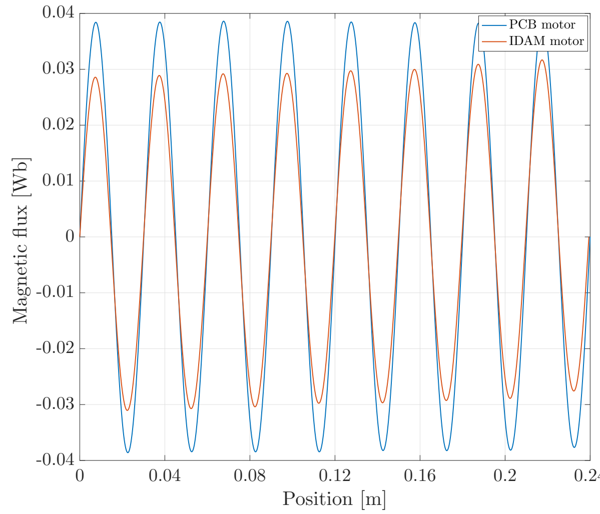

Fig. 14. Evolution of magnetic flux with position.

from the the non-ideal contact between the layers since an error of approximately 10% is observed by measuring the phase resistance of one PCB layer. This error of 10% can be explained by the impact of the vias [7], that are not taken into account in the model, and by the actual thickness of the copper tracks, which is slightly lower than expected. Ultimately, the motor constant is 16% smaller than the value that was predicted by the model. The theoretical and experimental values are summarized in Table IV. It has to be noticed that, due to the manufacturing process of the winding layers, the theoretical value of the motor constant is 9% smaller than the value presented in Section IV.

In Table V, the values of the force constant and of the phase resistance for both motors are summarized. Deriving the motor constants from these two parameters shows a remarkable achievement: the proposed motor has a motor constant that is approximately two times higher than the motor constant of the commercial motor.

TABLE IV
PROPOSED MOTOR PARAMETERS

Parameter	**Symbol**	**Theoretical value**	**Experimental value**
Phase resistance	R_{ph}	2.8 $[\Omega]$	3.5 $[\Omega]$
Force constant	k_f	17.8 $[N/A_{rms}]$	17.04 $[N/A_{rms}]$
Motor constant	k_p	7.54 $[N/\sqrt{W}]$	6.44 $[N/\sqrt{W}]$

TABLE V
COMPARISON BETWEEN BOTH MOTORS

Motors	R_{ph}	k_f	k_p
Proposed motor	3.5 $[\Omega]$	17.04 $[N/A_{rms}]$	6.44 $[N/\sqrt{W}]$
Commercial motor	11.8 $[\Omega]$	13.2 $[N/A_{rms}]$	3.84$[N/\sqrt{W}]$

VI. CONCLUSION

In this paper, the potential of the flex-PCB technology for obtaining high dynamic and high precision actuator has been investigated. To that end, an electromagnetic model of the actuator has been presented. This model consider a set of assumptions, which allows to simplify the original problem to a 2D problem. However the validity of the hypotheses has been confirmed by comparing the results obtained with the proposed model with FEM models. From this model, the motor constant has been derived as the performance criterion related to the force density. Regarding the oscillations on the force, a comparison of several indexes revealed that the criterion relying on the harmonic content of the magnetic flux is not the most suitable. A bi-objective optimization, combining the two most relevant optimization criteria has been realized. One important result of this optimization process is a Pareto front, from which one motor can be selected, depending on the application. Finally, a prototype of the winding has been realized and characterized using a designed test bench. From a simultaneous measurement of the back-emf and of the position, the magnetic flux with respect to the position has been derived. Performing a Fourier analysis allowed to find the force constant. Combining this with a measure of the electrical resistance, showed an error of 16 $\%$ on the motor constant, mainly due to the error on the resistance. However, the measurement system was not accurate enough to provide a measure of THD_{Ψ}. Nevertheless, the predictions from the models are confirmed by the experimental measurements.

A commercial motor has also been selected and its performances have been compared to the considered motor. The results of the study have shown that the proposed motor can achieve a motor constant that is two times higher, which clearly validates the potential of the PCB technology for obtaining high-dynamic and high-precision actuators.

REFERENCES

[1] Z. O. Zhu, Z. P. Xia, D. Howe, and P. H. Mellor. Reduction of cogging force in slotless linear permanent magnet motors. *IEE Proceedings - Electric Power Applications*, 144(4):277–282, July 1997.

[2] Gyu-Hong Kang, Jung-Pyo Hong, and Gyu-Tak Kim. A novel design of an air-core type permanent magnet linear brushless motor by space harmonics field analysis. *IEEE Transactions on Magnetics*, 37(5):3732–3736, Sep. 2001.

[3] N. Fujii and K. Okinaga. X-y linear synchronous motor without force ripple and core loss for precision two-dimensional drive. pages GU13–, April 2002.

[4] L. Hsu, G. Yan, and M. Tsai. Novel flexible printed circuit windings for slotless linear motor design. pages 1578–1582, Oct 2010.

[5] F. Baudart, B. Dehez, J. Denies, M. Markovic, and Y. Perriard. Shape optimization of flexible pcb slotless windings in bldc machines. pages 943–948, Oct 2013.

[6] B. Dehez, F. Baudart, and Y. Perriard. Analysis of a new topology of flexible pcb winding for slotless bldc machines. pages 1–8, May 2017.

[7] B. Dehez, F. Baudart, M. Markovic, and Y. Perriard. Theoretical and experimental investigation of flex-pcb air-gap windings in slotless bldc machines. *IEEE Transactions on Industry Applications*, 50(5):3153–3160, Sep. 2014.

[8] D. Imstepf, F. Baudart, Y. Perriard, and B. Dehez. Potential of flex-pcb winding in coreless tubular permanent magnet synchronous machines. pages 1–7, Nov 2016.

[9] B. L. J. Gysen, K. J. Meessen, J. J. H. Paulides, and E. A. Lomonova. General formulation of the electromagnetic field distribution in machines and devices using fourier analysis. *IEEE Transactions on Magnetics*, 46(1):39–52, Jan 2010.

[10] X. Liu and S. Huang. Magnetic field and thrust analysis of the u-channel air-core permanent magnet linear synchronous motor. pages 1–1, Nov 2016.

[11] M. F. J. Kremers, J. J. H. Paulides, J. L. G. Janssen, and E. A. Lomonova. Design considerations for coreless linear actuators. *IEEE Transactions on Magnetics*, 49(5):2271–2274, May 2013.

[12] G. François, F. Baudart, and B. Dehez. Analytical estimation of eddy current losses in pcb winding for the optimal sizing of pm slotless motor. pages 862–869, May 2019.